

## Dust Emission as a Function of Stellar Population Age in the Nearby Galaxy M33

KATE MALLORY,<sup>1</sup> DANIELA CALZETTI,<sup>1</sup> AND ZESEN LIN<sup>2,3</sup>

<sup>1</sup>*Department of Astronomy, University of Massachusetts Amherst, 710 North Pleasant Street, Amherst, MA 01003, USA*

<sup>2</sup>*CAS Key Laboratory for Research in Galaxies and Cosmology, Department of Astronomy, University of Science and Technology of China, Hefei 230026, People's Republic of China*

<sup>3</sup>*School of Astronomy and Space Science, University of Science and Technology of China, Hefei 230026, People's Republic of China*

### ABSTRACT

Dust emission at  $8\ \mu\text{m}$  has been extensively calibrated as an indicator of current star formation rate for galaxies and  $\sim\text{kpc}$ -size regions within galaxies. Yet, the exact link between the  $8\ \mu\text{m}$  emission and the young stellar populations in galaxies is still under question, as dust grains can be stochastically heated also by older field stars. In order to investigate this link, we have combined mid-infrared images from the *Spitzer Space Telescope* with a published star cluster candidates catalog for the Local Group galaxy M33. M33 is sufficiently close that the *Spitzer's*  $8\ \mu\text{m}$  images resolve individual regions of star formation. Star clusters represent almost-single-age stellar populations, which are significantly easier to model than more complex mixtures of stars. We find a decrease in the  $8\ \mu\text{m}$  luminosity per unit stellar mass as a function of age of the star clusters, with a large scatter that is consistent with varying fractions of stellar light absorbed by dust. The decrease and scatter both confirm findings based on more distant galaxies and are well described by simple models for the dust emission of a young stellar population. We conclude that the dust emission at  $8\ \mu\text{m}$  depends sensitively on the age of the stellar population, out to at least the oldest age analyzed here,  $\sim 400\ \text{Myr}$ . This dependence complicates the use of the  $8\ \mu\text{m}$  emission as a star formation rate indicator, at least for small galactic regions and individual star forming regions. By leveraging the *Spitzer* legacy, this investigation paves the way for future explorations with the *James Webb Space Telescope*.

*Keywords:* Interstellar Dust: Polycyclic Aromatic Hydrocarbons; Disk Galaxies: M33 (Triangulum Galaxy); Young Star clusters

### 1. INTRODUCTION

Star formation occurs in dusty environments, and most of the ultraviolet (UV) and optical light emitted by the young stars is absorbed by dust and re-emitted in the mid- and far-infrared, at  $\lambda > 3\ \mu\text{m}$ . Thus infrared emission can effectively trace the star formation in galaxies and regions within galaxies. For this reason, much effort has been expended over the past few decades to calibrate the infrared emission as a star formation rate (SFR) tracer (see review by Kennicutt & Evans 2012).

The mid-infrared ( $\lambda \sim 3\text{--}30\ \mu\text{m}$ ) emission is particularly attractive for tracing recent star formation, as it can be targeted by infrared facilities out to moderate redshifts. Samples of galaxies out to  $z \approx 2$  were secured by observations in the restframe mid-infrared with the *Spitzer Space Telescope* (*Spitzer* henceforth, Werner et al. 2004) and the *Herschel Space Observatory* (e.g., Reddy et al. 2006, 2010; Elbaz et al. 2011; Shivaei et al. 2015; Shipley et al. 2016; Shivaei et al. 2017); higher redshift populations, using the bluest mid-infrared features, can potentially be secured with the recently launched James Webb Space Telescope due to its higher sensitivity relative to the other telescopes.

The mid-infrared region is dominated by emission from Polycyclic Aromatic Hydrocarbons (PAHs) and small dust grains stochastically heated by a wide range of photon energies in the galaxy's radiation field (Leger & Puget 1984; Draine & Li 2007; Tielens 2008). The PAH molecules, which produce  $\sim 5\text{--}10\%$  of the total infrared emission (Smith et al. 2007), are excited by UV photons in the wavelength range  $\sim 0.0912\text{--}0.2\ \mu\text{m}$  and emit in a series of features between  $3\ \mu\text{m}$  and  $\sim 20\ \mu\text{m}$ . These include the strong  $\sim 7.7\ \mu\text{m}$  emission feature which dominates the band targeted by the *Spitzer/IRAC*  $8\ \mu\text{m}$  array (Fazio et al. 2004) and has been extensively calibrated as a SFR tracer (e.g., Wu et al. 2005; Reddy et al. 2006; Kennicutt et al. 2009; Shipley et al. 2016). As discussed in Shipley et al. (2016), calibrations

from different authors are generally consistent with each other within  $\sim 0.2$  dex, when using samples of metal-rich galaxies dominated by recent star formation ( $\text{SFRs} > \text{a few } M_{\odot} \text{ yr}^{-1}$ ).

PAHs, however, are also fragile molecules that are destroyed in the high-energy environments of massive star formation and AGNs, requiring shielding from large dust grains to survive (Madden et al. 2006; Gordon et al. 2008; Lebouteiller et al. 2011; Binder & Povich 2018). For this reason, PAH emission is mainly found in the Photodissociation Regions surrounding star forming regions and in the diffuse interstellar medium (Povich et al. 2007; Bendo et al. 2008; Relaño & Kennicutt 2009; Tielens 2013). In local galaxies, between 30% and 80% of the emission at  $8 \mu\text{m}$  is diffuse, found outside of regions that actively form stars (Boselli et al. 2004; Crocker et al. 2013; Calapa et al. 2014; Lu et al. 2014).

The complexity of the response of the PAH features to heating and excitation is compounded by their strong sensitivity to the metal abundance of the interstellar medium (e.g., Engelbracht et al. 2008). Their intensity becomes negligible below oxygen abundances  $\sim 0.2$  solar (Aniano et al. 2020), which has been interpreted as due to the formation mechanism (Sandstrom et al. 2012) or processing of the carriers by the environment (Madden et al. 2006; Gordon et al. 2008). These dependencies ultimately have complicated a robust calibration of the  $8 \mu\text{m}$  emission as a SFR tracer (Calzetti et al. 2007).

One approach to disentangling the different effects acting on PAHs is to gauge the response of their emission to stellar populations with ‘controlled’ parameters. Star clusters, by approximating single-age populations (Wofford et al. 2016), offer convenient ‘controlled’ templates for such analysis. They are abundant in galaxies, thus yielding the power of statistics, and cover a wide range of ages, from just formed systems to ancient sources almost as old as the Universe (e.g., Adamo & Bastian 2018). The age of a stellar population is directly linked to its UV output (Leitherer et al. 1999), thus providing a tracer for this parameter.

Recently, Lin et al. (2020) investigated the  $8 \mu\text{m}$  emission from 97 star clusters across 5 galaxies within 5 Mpc. The sample these authors use is from the LEGUS project (Calzetti et al. 2015), which provided catalogs of ages, masses, and extinctions for  $\sim 15,000$  star clusters in 50 galaxies closer than  $\sim 16$  Mpc, using multiband *Hubble Space Telescope* imaging (Adamo et al. 2017). Lin et al. (2020) restricted their sample to nearby galaxies and relatively isolated star clusters to minimize superposition between sources measured with the lower-resolution *Spitzer* and to mitigate contamination of the cluster emission from the surrounding stellar populations. Using their final sample of 97 star clusters, the authors find a clear anti-correlation between the mass-normalized  $8 \mu\text{m}$  luminosity of the star clusters and their age, indicating that the PAH emission directly responds to the presence of UV photons. The authors also show that the anti-correlation can be easily explained with simple models for the stellar populations combined with dust emission. They explain the significant scatter,  $\sim 1$  dex, in their data as combined effects of varying dust absorption fractions of the UV light and varying PAH abundances. Despite the careful selection, Lin et al. (2020) still cannot completely avoid potential effects of contamination of the observed  $8 \mu\text{m}$  emission from the stellar populations surrounding the star clusters.

In this paper, we seek to expand upon the investigation of Lin et al. (2020) by analyzing the  $8 \mu\text{m}$  emission of the star clusters in the Local Group galaxy M33. M33 (NGC598, Triangulum Galaxy) is located at a distance of 850 kpc (Ferrarese et al. 2000), implying that the  $2''$  full width at half maximum (FWHM) of the *Spitzer*/IRAC  $8 \mu\text{m}$  Point Spread Function subtends about 8 pc in spatial scale. M33 is an Sc spiral galaxy with a modest inclination of  $52^{\circ}$  (Figure 1; Corbelli & Salucci 2000) and significant star formation ( $\text{SFR} \simeq 0.5 M_{\odot} \text{ yr}^{-1}$ , Verley et al. 2009). Its proximity enables us to study the  $8 \mu\text{m}$  emission from star clusters while drastically reducing the possibility of confusion from multiple sources along the line of sight. We are also able to reach fainter  $8 \mu\text{m}$  luminosities than was possible with the data used by Lin et al. (2020) and can better quantify the scatter at fixed age observed by these authors.

The paper is organized as follows. Section 2 presents the imaging data used in this work and the source of the star cluster catalog; Section 3 details the photometric measurements performed on the images; Section 4 describes the models used for the comparison with the data; finally, in Section 6 and Section 7 we discuss our results and our conclusions, respectively.

## 2. DATA SOURCES AND CHARACTERISTICS

The infrared images of M33 obtained with the *Spitzer*/IRAC instrument were first presented by McQuinn et al. (2007). The images used in this study are those taken with the  $3.6 \mu\text{m}$  and  $8.0 \mu\text{m}$  filters. They were retrieved from the NASA Extragalactic Database (NED); the images are mosaics constructed by combining several frames, which provide a contiguous view of this large galaxy with a pixel scale of  $0''.75/\text{pixel}$  and at a resolution (FWHM) of  $\sim 1''.7$

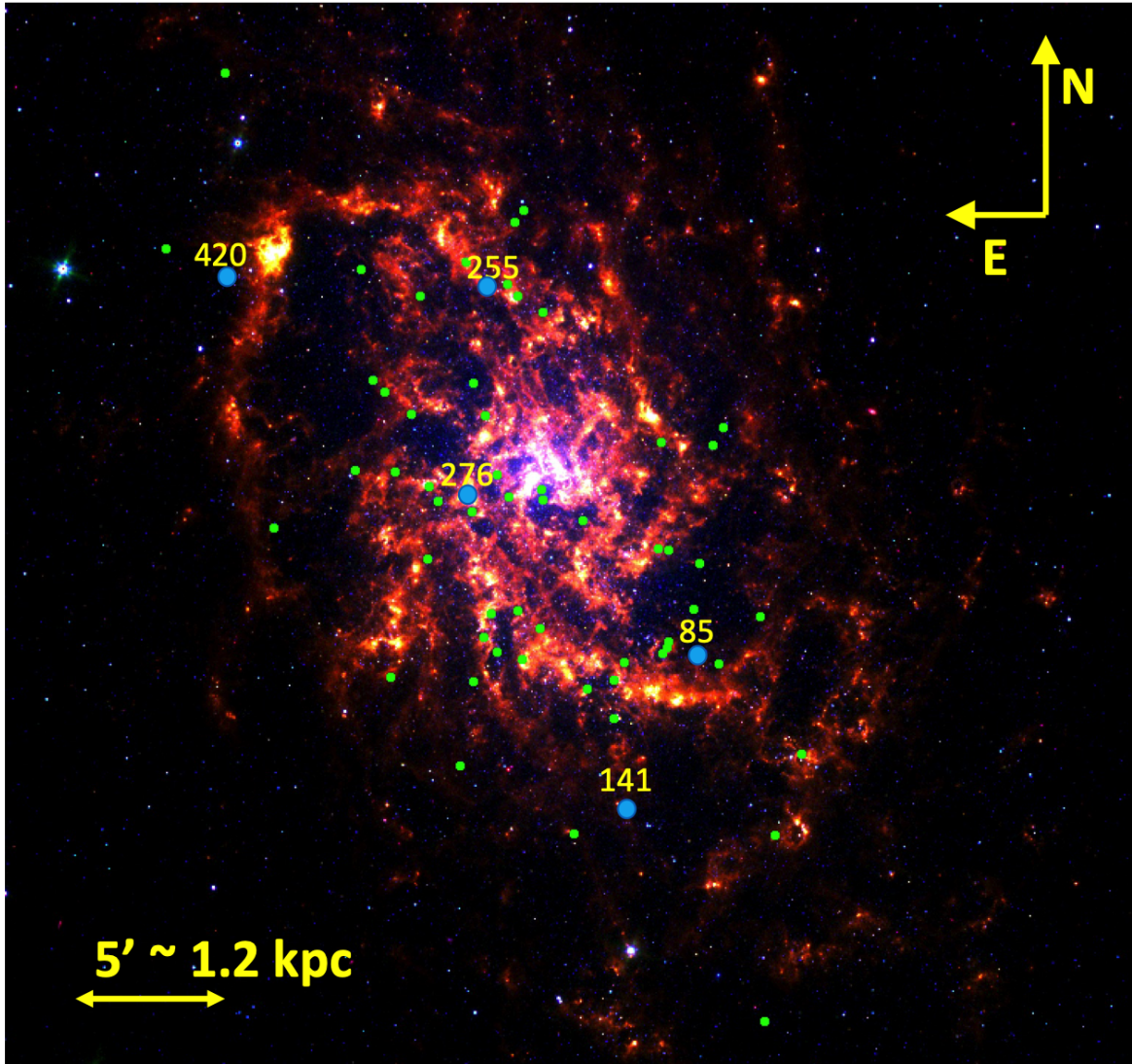


**Figure 1.** A three-color image of the galaxy M33, at a distance of  $\sim 850$  kpc, obtained by combining the  $4.5 \mu\text{m}$  (blue),  $5.8 \mu\text{m}$  (green), and  $8.0 \mu\text{m}$  (red) bands from the *Spitzer*/IRAC instrument. The scale of the image and orientation are shown on the figure. The 63 star clusters from the compilation of Sarajedini & Mancone (2007) used in this study are marked with green dots on the image. The five star clusters shown in detail in Figure 2 are marked with larger cyan dots and their IDs from Sarajedini & Mancone (2007) given on the galaxy image.

and  $\sim 2''$  for the  $3.6 \mu\text{m}$  and  $8.0 \mu\text{m}$  images, respectively (Dale et al. 2009). At the distance of M33 (previous section), these FWHMs correspond to physical scales of 7.0 pc and 8.2 pc at  $3.6 \mu\text{m}$  and  $8.0 \mu\text{m}$ , respectively. The  $3.6 \mu\text{m}$  image is used in this work exclusively to trace and remove the stellar contribution from the  $8.0 \mu\text{m}$  emission, as described in the section 3. The catalog of star clusters is taken from the compilation of Sarajedini & Mancone (2007), which is described in the next section.

### 3. DATA ANALYSIS

Sarajedini & Mancone (2007) classified sources in M33 into three categories: individual stars, star clusters, and unknown objects. Their compilation lists a total of 451 sources, including 255 confirmed clusters from *Hubble Space Telescope* or high-resolution ground imaging. In addition to the classification, the authors provide the coordinates of the sources and, for many, optical photometry, ages and masses compiled from the literature (see Sarajedini & Mancone 2007, for a list of references). Briefly, the ages and masses are derived from fits with stellar population models of the  $0.38\text{--}1 \mu\text{m}$  spectral energy distributions in eight medium-band filters (e.g., Ma et al. 2001).

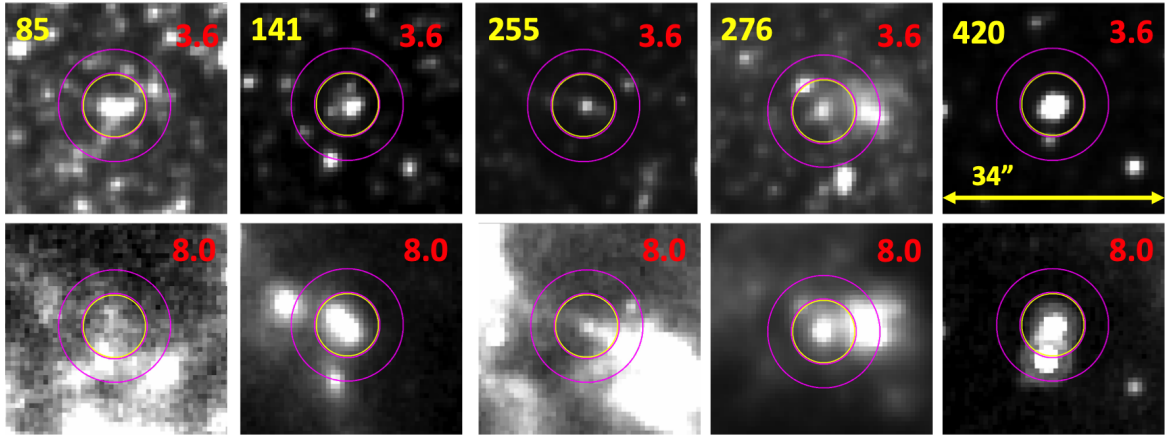


**Figure 2.** Cutouts of the IRAC  $3.6 \mu\text{m}$  (top row) and  $8 \mu\text{m}$  (bottom row) images centered on the five sources marked in Figure 1, showing the apertures (yellow circles) and the background annuli (magenta circles) used for the photometric measurements. The numbers given in the cutouts refer to the source IDs listed in Table 1. Sarajedini & Mancone (2007) classify # 141 and # 276 as ‘unknowns’, while the other three are confirmed star clusters. Each cutout is  $34''$  in size, as also indicated in the last panel to the right. The morphologies and behavior of the five clusters are representative of those of the overall sample of 63 sources.

We down-selected the Sarajedini & Mancone (2007) catalog as follows. We omitted all stars and several unknown sources which appeared to have stellar profiles from visual inspection of the optical images <sup>1</sup>. Furthermore, we only selected sources that listed both ages and masses, and were younger than 400 Myr (i.e.,  $\log(\text{age}/\text{yr}) < 8.6$ ). The latter constraint was imposed because older clusters are usually devoid of dust (Whitmore et al. 2020); for instance, Lin et al. (2020)’s sample only contains one cluster older than 400 Myr with detectable  $8 \mu\text{m}$  emission at its location. An inspection of the stellar continuum-subtracted  $8 \mu\text{m}$  image confirms that old clusters are generally coincident with non-detections. We finally removed all sources that are too faint to show emission at  $8.0 \mu\text{m}$  and  $3.6 \mu\text{m}$ . After trimming the list based on these criteria, we are left with 63 sources, which generally show a compact morphology at  $8 \mu\text{m}$ . These sources are listed in Table 1 together with the identification numbers, locations, ages, masses, and classification from Sarajedini & Mancone (2007). Of the 63 sources, 13 are classified as ‘unknown’ by those authors, while the rest are star clusters. We retain the 13 unknown sources since they show characteristics similar to those of the other star clusters. We note that Sarajedini & Mancone (2007) do not report uncertainties for their parameters. The locations of the 63 sources in M33 are indicated in Figure 1 with green and cyan dots. As expected for young star clusters, the sources are mainly located along the spiral arms, with 59/63 within 4 kpc of the center.

Aperture photometry at both  $3.6 \mu\text{m}$  and  $8.0 \mu\text{m}$  was then performed with Astroconda, using a circular aperture centered on each candidate cluster. The aperture radii were chosen to be the same for both bands and for all clusters. We select an aperture radius of 6.67 pixels ( $5''.0$ ,  $\sim 21 \text{ pc}$ ) as an optimal compromise between the extent of the observed  $8 \mu\text{m}$  emission and the need to avoid neighboring sources and inclusion of excess noise from the background. For measuring the background, we elect to use an annulus with inner radius of 7 pixels ( $5''.25$ ) and a width of 5 pixels ( $3''.75$ ). The goal of the annulus is to capture the local background values around each star cluster, with sufficient statistics to mitigate the noise in this measurements. In our case, the annulus includes about two times more pixels than the photometric aperture, thus reducing by  $\sqrt{2}$  the noise level added by this component to the final measurement; the value of the background is calculated as the mode of the pixels’ values, after implementing 10 iterations with  $3\text{-}\sigma$  clipping in order to remove the contribution of any bright source in the annulus. Examples of sources with the photometric apertures and sky annuli drawn on IRAC  $3.6 \mu\text{m}$  and  $8 \mu\text{m}$  image cutouts are given in Figure 2. The local background in the two images includes both the diffuse stellar light and diffuse dust emission (PAHs and stochastically heated dust) from the galaxy; by removing these, we concentrate on the stellar and dust emission associated with each star cluster. The  $3.6 \mu\text{m}$  image may still contain hot dust emission heated by the young stars, but we expect this to only affect clusters younger than 10 Myr (Whitmore et al. 2011) and to represent a small fraction of the background-subtracted  $3.6 \mu\text{m}$  emission (Querejeta et al. 2015). For all practical purposes, the background-subtracted

<sup>1</sup> also available from NED.

3.6  $\mu\text{m}$  photometry captures the stellar light from the star clusters. The measured flux densities,  $f_{3.6}$  and  $f_{8.0}$ , in the default units of MJy/sr of the *Spitzer* images, are listed in Table 1.

We apply aperture corrections to our measurements, in order to account for the flux in the wings of the cluster emission that is lost due to the finite size of the aperture used for the photometry. While the 3.6  $\mu\text{m}$  photometry is dominated by the photospheric emission of the stars in the cluster (see above), the 8  $\mu\text{m}$  photometry is the sum of contributions from stellar light and dust emission. Star clusters are compact sources, whose stellar distributions have typical sizes of  $\sim 3$  pc (Ryon et al. 2017; Brown & Gnedin 2021). Conversely, the dust emission that surrounds the clusters is expected to be extended, as the UV photons that heat the dust can travel several tens of pc from the stars that produce them (Relaño & Kennicutt 2009; Lawton et al. 2010). Because of this difference in behavior, aperture corrections for the dust emission at 8  $\mu\text{m}$  are calculated after removing the stellar emission from this band.

At the distance of M 33, the typical size of star clusters translates to an angular size of  $\sim 0.7''$ , much smaller than the IRAC  $\sim 2''$  Point Spread Function. Thus, for practical purposes, the stellar emission from our clusters can be considered originating from a point source. Table 4.8 of the IRAC Instrument Handbook <sup>2</sup> lists aperture corrections of  $\sim 7\%$  and  $\sim 9\%$  for a point source measured in our default aperture radius ( $5''.0$ ) at 3.6  $\mu\text{m}$  and 8  $\mu\text{m}$ , respectively. We neglect, in what follows, the small 2% difference in correction between the two bands for the stellar emission.

The dust-only 8  $\mu\text{m}$  emission is calculated as:  $f_{8.0,\text{dust}} = (f_{8.0} - 0.23f_{3.6})$ , following Helou et al. (2004). As explained by these authors, the factor 0.23 applied to the 3.6  $\mu\text{m}$  flux density rescales the stellar emission to its equivalent intensity at 8  $\mu\text{m}$ , according to the Starburst99 stellar population models (Leitherer et al. 1999); the rescaled stellar component is then subtracted from the observed 8  $\mu\text{m}$  flux density to extract the dust-only 8  $\mu\text{m}$  emission. To establish the aperture corrections for the dust emission, we perform photometry on 9 isolated clusters for increasing radii, from 6.67 pixels (our default aperture radius) to 20 pixels ( $15''$ ,  $\sim 60$  pc). The maximum radius comfortably encloses a typical H II region while ensuring that neighboring sources are not included in the measurements. The growth curves, normalized to the photometry in the default aperture (6.67 pixels) are shown in Figure 3 for the dust-only 8  $\mu\text{m}$  emission. We adopt the average of the growth curves at 20 pix as the mean aperture correction for our measurements; this correction increases our dust-only 8  $\mu\text{m}$  photometric measurements by a factor of 3.95. As a sanity check, we compare our aperture corrections with those derived by Lin et al. (2020), taking into account the differences in galaxy distances and aperture sizes between the two studies. We find that, when using closely matched *physical* sizes for the apertures, the 8  $\mu\text{m}$  aperture correction of Lin et al. (2020) is a factor  $\sim 10\%$  smaller than our derived correction factor. We attribute the small difference to the higher spatial resolution of our study, which allows us to better sample the dynamical range of the dust-emitting regions.

We convert the dust flux density to a luminosity at 8  $\mu\text{m}$ ,  $L_{8.0}$ , by multiplying the aperture-corrected flux density for the effective frequency of the 8  $\mu\text{m}$  band ( $3.81 \times 10^{13}$  Hz), using the distance of 850 kpc for M33. As our sources are extended, we include an additional correction factor 0.86 for light scattering into the IRAC instrument, which is appropriate for the largest aperture,  $15''$ , used to calculate the curve of growth<sup>3</sup>. The list of luminosities, corrected as described so far, is given in Table 1, in units of  $\text{erg s}^{-1}$ . For the purpose of our analysis, these are converted to luminosities in solar units by dividing  $L_{8.0}$  for the Sun's luminosity of  $3.826 \times 10^{33}$   $\text{erg s}^{-1}$ .

Measurement errors are dominated by uncertainties in the centering of the photometric apertures on sources in the IRAC images. The errors were estimated by ‘wiggling’ the photometric aperture around seven representative regions by  $\pm 3$  pixels (about one resolution element in the 8  $\mu\text{m}$  image) around the nominal centers and re-measuring photometry at both 3.6  $\mu\text{m}$  and 8  $\mu\text{m}$ . The resulting flux variations are then combined to propagate the uncertainty to the dust-only  $L_{8.0}$ . This uncertainty, at the level of 0.17 dex, is adopted as our measurement uncertainty for all sources.

#### 4. DESCRIPTION OF MODELS

We employ the models produced by Lin et al. (2020) to compare our measurements with expectations for the dust emission of young star clusters. These authors combined the Starburst99 models (Leitherer et al. 1999; Vázquez & Leitherer 2005) for the stellar populations with the Draine & Li (2007) models for the dust emission. We give below a short description of the assumptions used by Lin et al. (2020) for both sets of models, and the quantities these authors derived for comparison with measurements and which will be used for the present study, as well.

<sup>2</sup> <https://irsa.ipac.caltech.edu/data/SPITZER/docs/irac/iracinstrumenthandbook/>

<sup>3</sup> section 8.2 of the IRAC Instrument Handbook: <https://irsa.ipac.caltech.edu/data/SPITZER/docs/irac/iracinstrumenthandbook/>

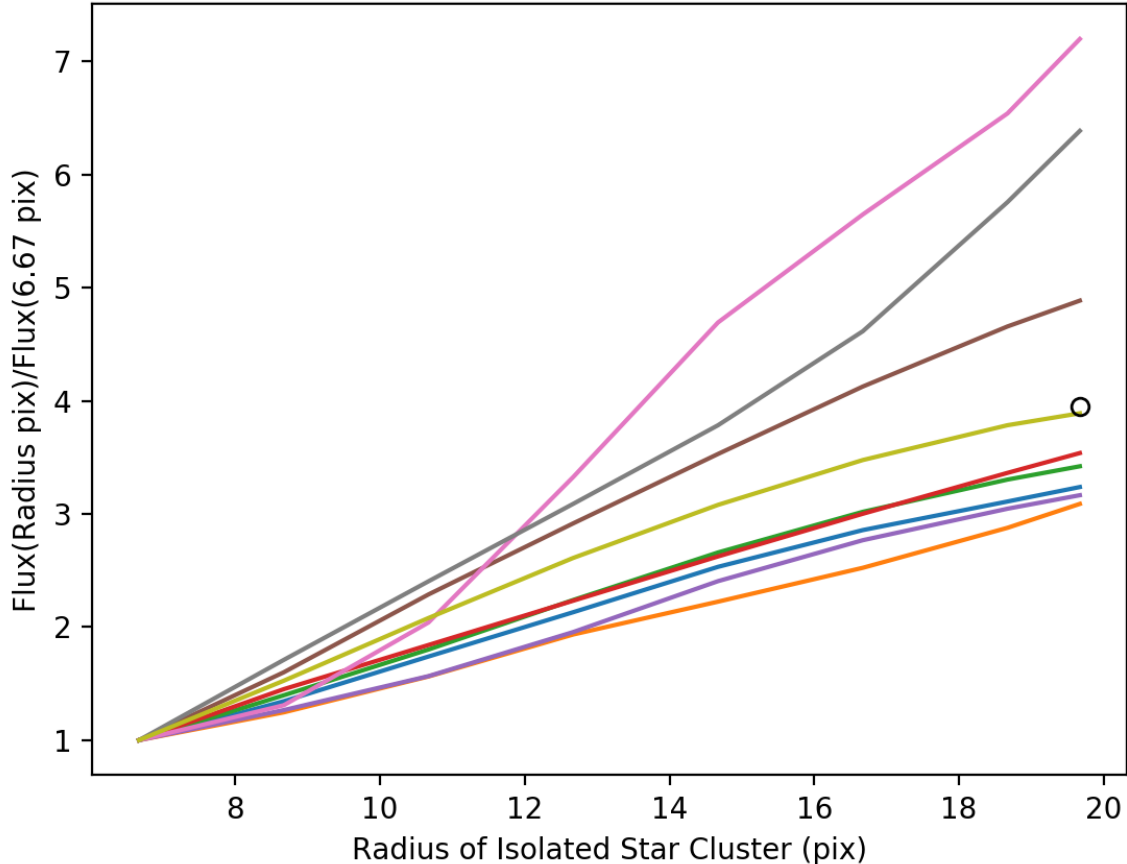


**Figure 3.** Growth curves for 9 isolated clusters in the  $8\ \mu\text{m}$  image of M33, for increasing radii from our default value of 6.67 pix ( $5''$ ) out to 20 pix ( $15''$ ). The curves are derived from flux measurements at the indicated radii normalized to the flux in the default aperture. The open black circle is the average of the curves at 20 pix, which we adopt as the  $8\ \mu\text{m}$  aperture correction for our photometric measurements.

Spectral energy distributions (SEDs) of stellar population models were generated by Lin et al. (2020) for both instantaneous burst and constant star formation models in the age range 1–500 Myr, with a metallicity range  $Z = 0.004 - 0.02$  (with  $Z_{\odot} = 0.014$ ), and covering several stellar evolutionary tracks. Instantaneous bursts are considered reasonable representations of the stellar populations contained in star clusters (Wofford et al. 2016). The model SEDs were then integrated in the wavelength range  $0.0912-2\ \mu\text{m}$  to produce the expected dust emission:  $L(\text{TIR}) = f_{\text{abs}} \times L(0.0912-2)$ , where  $L(\text{TIR})$  is the infrared emission in the range  $3-1000\ \mu\text{m}$ ,  $L(0.0912-2)$  is the stellar light in the UV-to-nearIR range, and  $f_{\text{abs}}$  gives the fraction of the stellar light that is absorbed by the dust and re-emitted in the infrared.  $f_{\text{abs}} = 1$  means that 100% of the UV-to-nearIR stellar light from a star cluster is absorbed by dust; this is clearly a strict upper limit and unlikely to be generally true for our clusters, since they are all detected at optical wavelengths (Sarajedini & Mancone 2007).

The Draine & Li (2007) models were used to calculate the fraction of  $L(\text{TIR})$  emitted at  $8\ \mu\text{m}$ . The shape of the dust SED depends on various parameters, including the grain size distribution, the PAH abundance ( $q_{\text{PAH}}$ ), and the intensity of the starlight heating the dust. For the latter, Draine & Li (2007) use the dimensionless parameter  $U$ , which is the intensity of the local radiation field normalized to the radiation field intensity of the solar neighborhood. Lin et al. (2020) calculated a set of  $L_{8.0}/L(\text{TIR})$  ratios assuming the grain size distribution of the Milky Way, a fixed value for  $U = 12$ , and a range of PAH abundances from  $q_{\text{PAH}} = 0.47\%$  to  $4.58\%$ . The latter value,  $4.58\%$ , is the highest available from the models and is consistent with the value observed in our own Milky Way.

Lin et al. (2020) produced trends of the mass-normalized  $L_{8.0}$  of a star cluster as a function of the cluster’s age. The dependence of  $L_{8.0}$  on stellar mass is a trivial one: lighter clusters contain proportionally less stars, thus less stellar light that can be processed by dust into the infrared. Normalizing  $L_{8.0}$  by the cluster’s mass removes this trivial

dependence. The dependence on age is, conversely, more complex. For instantaneous burst SEDs, [Lin et al. \(2020\)](#) find that the PAH emission peaks at an age of  $\approx 3$  Myr and then decreases quickly from there. This is because young stellar populations have higher UV emission than older ones on account of the presence of massive stars; the sharp decrease beyond 3 Myr coincides with the most massive stars beginning to die off. The decreasing UV emission for ages  $> 3$  Myr causes a decrease in the amount of infrared emission that can be produced by the UV-heated dust and a corresponding decrease in the emission at  $8 \mu\text{m}$ . For the constant star formation models, the  $8 \mu\text{m}$  emission is enhanced relative to the instantaneous models at ages  $\geq 5$  Myr. However, like for the instantaneous model, the mass-normalized  $8 \mu\text{m}$  luminosity in the constant star formation model shows a steady decrease with increasing age. This is because, although massive, UV bright stars are continuously produced in this model, the stellar mass accumulates with time, thus steadily increasing the denominator of the  $L_{8.0}/M$  ratio.

After cluster age and mass, the next set of major dependencies for  $L_{8.0}$  are given by the PAH abundance ( $q_{\text{PAH}}$ ) and the fraction of stellar light absorbed by dust ( $f_{\text{abs}}$ ). These two parameters, which vary independently, only impact the scaling of the models for  $L_{8.0}/M$  as a function of cluster age, but not their shape. [Lin et al. \(2020\)](#) determines that  $L_{8.0}/L(\text{TIR})$  is weakly sensitive on  $U$  for the range of values expected in star-forming regions, and that changes in the properties of the stellar population models, e.g., metallicity and stellar evolutionary tracks, have negligible impact on the  $8 \mu\text{m}$  emission.

We consider Milky Way-like dust properties (Milky Way dust grain size distribution,  $q_{\text{PAH}} = 4.58\%$ ) appropriate for M33, because the oxygen abundances of the regions where the star clusters are located are within the range  $12 + \log(\text{O}/\text{H}) \sim 8.4 - 8.75$  ( $\sim 0.5 - 1.2$  solar)<sup>4</sup>, as measured from young stars and the gas ([U et al. 2009](#); [Bresolin 2011](#); [Toribio San Cipriano et al. 2016](#); [Lin et al. 2017](#)), and the PAH fraction is known to depend on metallicity ([Aniano et al. 2020](#)).

## 5. RESULTS

Prior to considering the mass-normalized  $8 \mu\text{m}$  emission, we analyze the luminosity,  $L_{8.0}$ , itself as a function of cluster age. This is shown in [Figure 4](#), where we find no correlation between these two quantities, as expected from the discussion in the previous section. The figure shows the individual star clusters as well as both the mean and median of the data binned in six groups of age. Given the large scatter in the original data, which is reflected in a large standard deviation in the binned data, there is no relevant trend observed for the  $8 \mu\text{m}$  luminosity also in the binned data. This confirms the argument presented in the previous section that the amount of dust emission from a star cluster depends not only on the presence of UV-emitting (young) stars, but also on the number of these stars, which is proportional to the total mass of the cluster if the stellar initial mass function is the same across all clusters.

Next, we turn to the mass-normalized  $8 \mu\text{m}$  emission,  $L_{8.0}/M$ , plotted as a function of the cluster’s age; this is shown in [Figure 5](#), where both clusters and the few sources classified as ‘unknown’ in [Sarajedini & Mancone \(2007\)](#) are plotted. The mass-normalized  $8 \mu\text{m}$  luminosity displays a clear inverse correlation for increasing cluster’s age. We overlay the models of [Lin et al. \(2020\)](#), discussed in [Section 4](#), on the data. The top-most model lines correspond to the case of instantaneous burst and continuous star formation populations with 100% of the UV-to-nearIR luminosity absorbed by dust and re-emitted in the infrared. These models mark the upper envelope to the data, similar to what observed by [Lin et al. \(2020\)](#) for their data. The observed trend has an immediate interpretation in light of the models. For instantaneous burst models, the younger clusters have more massive stars, implying larger amounts of UV emission to heat the dust, while the older clusters lose their massive stars so the dust is heated less effectively and the infrared (and  $8 \mu\text{m}$ ) emission per unit stellar mass decreases. For constant star formation models, younger clusters have lower masses and, thus, proportionally higher  $L_{8.0}/M$  than older clusters. Lower luminosity clusters at fixed age can be obtained by decreasing the fraction of UV luminosity absorbed by dust, which rigidly shifts the models downward. The lower end of the envelope is marked by model lines where only  $\sim 1\%$  of the UV/optical luminosity is processed by dust into the infrared (dashed lines in [Figure 5](#)).

## 6. DISCUSSION

Our main result is that the mass-normalized  $8 \mu\text{m}$  luminosity in star clusters and cluster candidates (the ‘unknown’ sources) sharply decreases for increasing age of the cluster population ([Figure 5](#)), thus confirming the results of [Lin et al. \(2020\)](#). Over a factor 125 in age increase, from  $\sim 3$  Myr to 400 Myr, the normalized  $8 \mu\text{m}$  luminosity decreases

<sup>4</sup> We adopt an oxygen abundance of  $12 + \log(\text{O}/\text{H}) = 8.69$  for the Sun ([Asplund et al. 2009](#)).

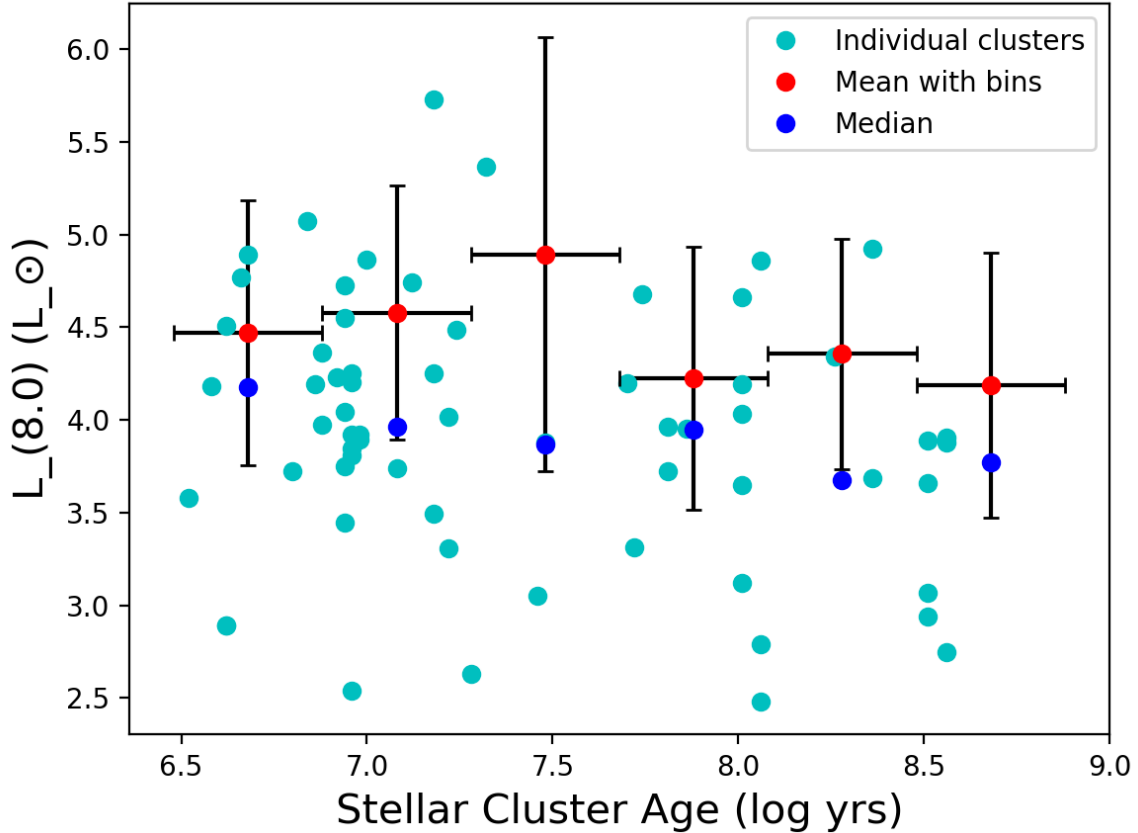


**Figure 4.** The dust-only  $8\ \mu\text{m}$  luminosity of each cluster as a function of age. The mean (red points, with the  $1\ \sigma$  standard deviation as black vertical lines) and the median (blue points) are shown for binned data, divided in six equal width bins in  $\log(\text{age})$ . The size of the bins is shown with horizontal black bars. The bins’ central values begin at  $\log(\text{age}/\text{yr}) = 6.68$  and increase in steps of 0.4 dex until the highest-age bin at  $\log(\text{age}/\text{yr}) = 8.68$ .

by about two orders of magnitude. At fixed age, our data show a significant a scatter, also of about two orders of magnitude. When compared with models for the expected dust emission of simple stellar populations, the data mostly fall below the  $f_{\text{abs}} = 1$  model lines, as expected since the models mark the upper envelope to the  $8\ \mu\text{m}$  luminosity. These models are derived under the assumption that 100% of the UV/optical luminosity generated by the stars in the clusters is absorbed by dust and re-emitted in the infrared. This is clearly an extreme behavior, as we expect (and it is observed) most star clusters to emit at least a fraction of their UV emission directly, without dust absorption. The observed scatter at fixed age is in line with this expectation; in Figure 5 we show the location of the same models, but under the condition that only 1% (lowest, dashed, model lines) of the UV/optical emission from the star clusters is absorbed by dust and re-emitted in the infrared. These two extreme model assumptions bracket the location of the vast majority ( $\sim 90\%$ ) of the data points within the uncertainties, indicating that the models are effective at explaining the observed behavior.

Although young star clusters are well represented by single stellar populations (Wofford et al. 2016), we note that some of our  $8\ \mu\text{m}$  luminosity estimates exceed the predictions of the instantaneous burst models for ages  $> 10^7$  yr and at high dust absorption fractions (blue solid line in Figure 5). There are 5 clusters (8% of total, magenta circles in Figure 5) whose mass-normalized  $8\ \mu\text{m}$  luminosity exceeds the topmost model prediction for instantaneous burst population by at least  $2\ \sigma$  and are better explained by constant star formation (cyan solid line in Figure 5). Lin et al. (2020) find a similar discrepancy between the strongest dust emitting clusters and instantaneous models in their sample. However, because of the distance of their targets (3.5–5 Mpc), Lin et al. (2020) cannot exclude that part of the observed excess may be due to blends of star clusters with different ages or contamination from the background population, which could artificially increase the observed  $8\ \mu\text{m}$  luminosity relative to the assigned cluster age. This type of contamination is not applicable to our homogeneous sample from a single very nearby galaxy where blends



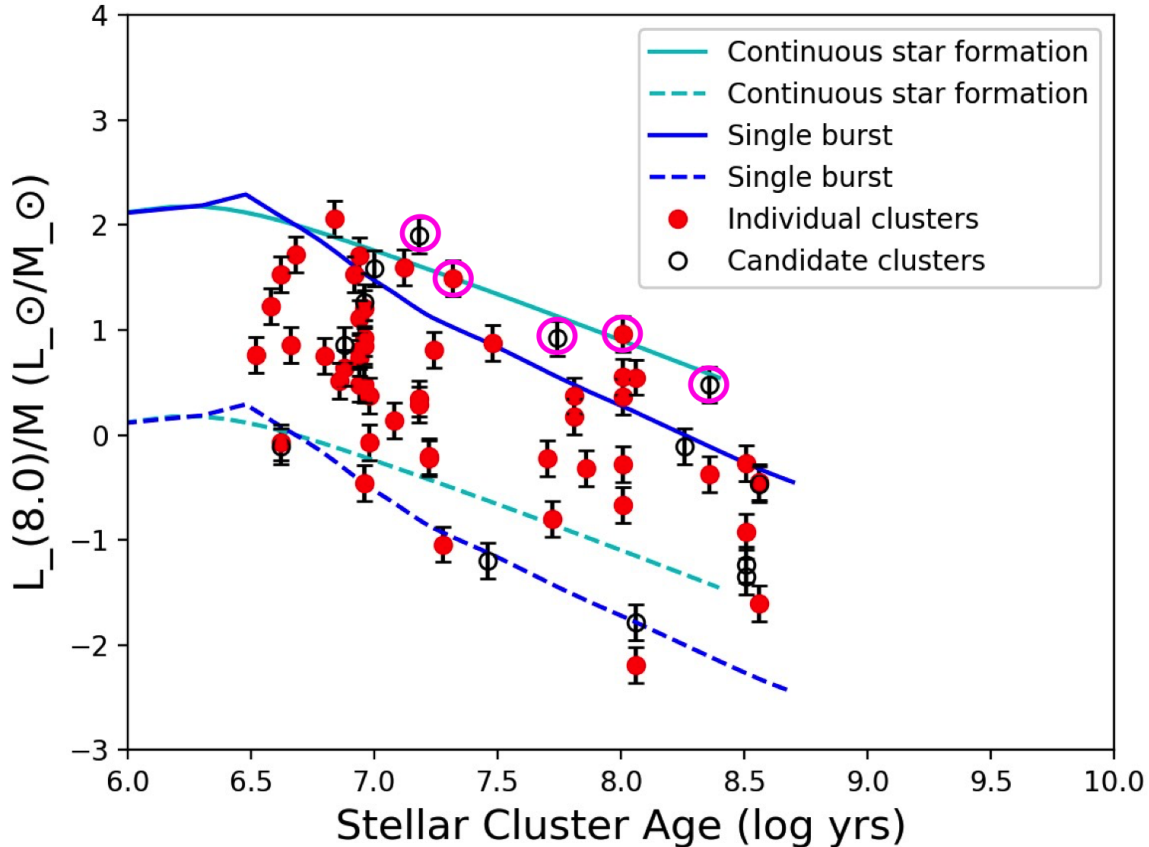


**Figure 5.** The dust-only  $8\ \mu\text{m}$  luminosity divided by the stellar mass,  $L_{8.0}/M$ , as a function of age for both clusters (red points) and ‘unknowns’ (black circles), shown together with their  $1\ \sigma$  uncertainties (black bars). The model expectations are shown for both the instantaneous, single burst (blue lines) and the constant star formation case (cyan lines). The top-most lines show the models’ location for the case  $f_{\text{abs}} = 1$ , i.e., that 100% of the cluster’s UV/optical light is absorbed by dust and re-emitted in the infrared. The lower lines show the location for  $f_{\text{abs}} = 0.01$ , i.e., only 1% of the UV/optical light is absorbed by dust. These models bracket the observations. Magenta circles identify the five clusters/unknowns whose values of  $L_{8.0}/M$  lie  $2\ \sigma$  or more above the prediction for the  $f_{\text{abs}} = 1$  single burst model.

of clusters can be easily recognized and removed. Furthermore, the emission from our star clusters is measured at  $\sim 20$  pc resolution, which removes much of the potential contamination from the background populations. If the four outliers were the result of constant star formation within the photometric aperture, the SFR of each region would be  $\lesssim 10^{-6}\ M_{\odot}\ \text{yr}^{-1}$ , sufficiently low that star formation would be sporadic (Weisz et al. 2012). We can therefore exclude constant star formation as an explanation for the five outliers.

We visually inspect the five outliers to garner additional insights into potential causes for their excess  $8\ \mu\text{m}$  luminosity. These outliers are two clusters (ID # 215 and 250) and three unknowns (ID # 107, 276 and 336) from Table 1. Source # 276 is shown in Figure 2; it is located near another, brighter source whose  $8\ \mu\text{m}$  emission wings spill over into the photometric aperture used for the source’s measurement. This morphology is representative of that presented by the other outliers as well. The proximity to brighter sources is likely to contribute to the observed excess in all five outliers.

There can be additional reasons for the excess dust emission of some star clusters relative to instantaneous model expectations. First and foremost, we do not have uncertainties for the ages and masses of our star clusters. While mass uncertainties for clusters in M33 are around several tens of percent, uncertainties in age determinations can be larger, in the range 0.1–0.3 dex (Moeller & Calzetti 2022). Adding such uncertainty to the ages, i.e., along the horizontal axis, would significantly reduce the discrepancy between data and instantaneous models. In addition, the ages of some of the clusters, which were derived from U-to-K band spectral energy distributions (e.g., Ma et al. 2001), may be overestimated, since age determinations are uncertain in the absence of either UV or line emission information (Whitmore et al. 2020). Furthermore, there may be uncertainties in the PAH models, which are still being updated

(Draine et al. 2020). Finally, star clusters may contain multiple-age stellar populations, generated over timescales of about 100 Myr (Bastian & Lardo 2018), which may affect age determinations from single-age models like Starburst99.

Our results expand over those of Lin et al. (2020) in two ways. Thanks to the proximity of M33, we expand by about an order of magnitude the luminosity range at fixed age towards fainter clusters. We do this across all ages, from 3 Myr to  $\sim 400$  Myr, which enables us to establish that, at fixed age, the mass-normalized  $8 \mu\text{m}$  emission covers a range of at least two orders of magnitude at all the ages probed here. We also increase about 5-fold (24 sources versus 5) the number of clusters in the age range  $10^7$ – $10^8$  yr, thus increasing the statistics in this age range and reinforcing the results of Lin et al. (2020).

Lin et al. (2020) attributes the range of mass-normalized  $8 \mu\text{m}$  emission at fixed age to two effects: (1) variations in  $f_{\text{abs}}$ , the fraction of stellar UV/optical light absorbed by dust; and (2) variations in the PAH fraction of the dust. In the present case, we can exclude that variations in PAH fraction play a significant role in the observed scatter of  $L_{8.0}/M$  at constant age. As discussed in Section 4, the oxygen abundance range at the location of our cluster sample is  $\sim 0.5$ – $1.2$  solar; adopting the dependence of the PAH fraction on oxygen abundance from Aniano et al. (2020), this range translates into a factor 2–3 variation in PAH abundance and a similar variation in  $8 \mu\text{m}$  luminosity (Lin et al. 2020). This is far below the two-orders-of-magnitude scatter of  $L_{8.0}/M$  at constant age observed in our data. The large scatter is more easily explained with variations in  $f_{\text{abs}}$  by a similar magnitude, from  $f_{\text{abs}} \sim 1$  to  $f_{\text{abs}} \sim 0.01$ .

## 7. CONCLUSIONS

The main result of this analysis is that the  $8 \mu\text{m}$  emission from dust displays a strong dependence on the age of the stellar population at young ages, decreasing by a factor  $\sim 100$  in mass-normalized intensity going from 3 Myr to  $\sim 400$  Myr. The decrease tracks expectations from models of emission from stars and dust, for a range of fractions of dust-absorbed UV/optical luminosity, from  $\sim 100\%$  down to  $\sim 1\%$ . This result can have important consequences for the detectability of galaxies at high redshift, where stellar populations tend to be young, although the dust fractions and PAH abundances tend to be low, lower than those found in a nearby galaxy like M33. Our study indicates that the  $8 \mu\text{m}$  luminosity can be effectively used as a tracer of the age of young stellar populations, although additional dependencies (metallicity, dust content, dust absorption fraction of the UV light, contamination from heating by older stellar populations, e.g., Calzetti et al. 2007) continue to complicate its use as a SFR indicator. In conclusion, we suggest that the  $8 \mu\text{m}$  dust emission should not be used as a SFR indicator for individual star-forming regions or small galactic regions, where stochastic effects in the star formation history can dominate. Comparisons between galaxies or between galaxy populations will need to take into account potential differences in their star formation histories.

The authors thank the anonymous referee for comments that have greatly improved the manuscript.

Based on archival data from the *Spitzer Space Telescope*, which was operated by the Jet Propulsion Laboratory, California Institute of Technology under a contract with NASA, and retrieved from the NASA/IPAC Infrared Science Archive, which is operated by the Jet Propulsion Laboratory, California Institute of Technology, under contract with NASA.

This research has also made use of the NASA/IPAC Extragalactic Database (NED) which is operated by the Jet Propulsion Laboratory, California Institute of Technology, under contract with the National Aeronautics and Space Administration.

Z. L. acknowledges support from the China Postdoctoral Science Foundation (2021M700137).

*Facilities:* Spitzer Space Telescope (IRAC)

*Software:* Astroconda (IRAF), SAOImage DS9, Python

**Table 1.**

| Region <sup>a</sup> | RA, DEC <sup>a</sup>   | Log (Age) <sup>a</sup> | Log (Mass) <sup>a</sup> | $f_{3.6}^b$     | $f_{8.0}^b$     | $L_{8.0}^c$           | Classification <sup>a</sup> |
|---------------------|------------------------|------------------------|-------------------------|-----------------|-----------------|-----------------------|-----------------------------|
| (1)                 | (J2000)<br>(2)         | (yrs)<br>(3)           | ( $M_{\odot}$ )<br>(4)  | (MJy/sr)<br>(5) | (MJy/sr)<br>(6) | ergs/s<br>(7)         | (8)                         |
| 42                  | 01:33:10.11 30:29:56.9 | 6.58                   | 2.95                    | 143.            | 72.8            | $5.91 \times 10^{37}$ | Cluster                     |
| 48                  | 01:33:14.29 30:27:11.1 | 6.96                   | 2.99                    | 13.7            | 50.4            | $6.99 \times 10^{37}$ | Unknown                     |
| 53                  | 01:33:16.10 30:20:56.0 | 6.96                   | 3.00                    | 8.29            | 2.82            | $1.36 \times 10^{36}$ | Cluster                     |
| 54                  | 01:33:16.63 30:34:35.7 | 8.01                   | 3.48                    | 21.0            | 33.3            | $4.21 \times 10^{37}$ | Cluster                     |
| 68                  | 01:33:22.32 30:40:59.4 | 8.36                   | 4.06                    | 8.30            | 14.7            | $1.90 \times 10^{37}$ | Cluster                     |
| 70                  | 01:33:23.10 30:33:00.5 | 7.86                   | 4.27                    | 20.5            | 28.2            | $3.47 \times 10^{37}$ | Cluster                     |
| 74                  | 01:33:23.90 30:40:26.0 | 6.92                   | 2.70                    | 46.3            | 55.3            | $6.61 \times 10^{37}$ | Cluster                     |
| 80                  | 01:33:26.00 30:36:24.3 | 8.51                   | 4.42                    | 26.6            | 9.18            | $4.55 \times 10^{36}$ | Unknown                     |
| 85                  | 01:33:26.75 30:33:21.4 | 7.08                   | 3.60                    | 24.1            | 20.0            | $2.14 \times 10^{37}$ | Cluster                     |
| 86                  | 01:33:26.94 30:34:52.6 | 6.94                   | 2.96                    | 27.1            | 13.5            | $1.08 \times 10^{37}$ | Cluster                     |
| 105                 | 01:33:31.00 30:36:52.6 | 6.96                   | 3.00                    | 35.7            | 30.1            | $3.24 \times 10^{37}$ | Cluster                     |
| 106                 | 01:33:31.10 30:33:45.5 | 7.81                   | 3.55                    | 23.0            | 19.2            | $2.05 \times 10^{37}$ | Cluster                     |
| 107                 | 01:33:31.22 30:33:33.5 | 7.74                   | 3.76                    | 16.5            | 130.            | $1.86 \times 10^{38}$ | Unknown                     |
| 113                 | 01:33:32.01 30:33:21.8 | 6.98                   | 3.52                    | 77.6            | 38.4            | $3.05 \times 10^{37}$ | Cluster                     |
| 114                 | 01:33:32.17 30:40:31.9 | 6.52                   | 2.81                    | 25.1            | 15.7            | $1.47 \times 10^{37}$ | Cluster                     |
| 119                 | 01:33:32.72 30:36:55.2 | 6.84                   | 3.01                    | 43.0            | 321.            | $4.61 \times 10^{38}$ | Cluster                     |
| 141                 | 01:33:37.60 30:28:04.6 | 8.36                   | 4.44                    | 34.3            | 228.            | $3.26 \times 10^{38}$ | Unknown                     |
| 144                 | 01:33:38.04 30:33:05.4 | 7.22                   | 3.51                    | 27.5            | 11.6            | $7.86 \times 10^{36}$ | Cluster                     |
| 152                 | 01:33:39.69 30:31:09.2 | 7.46                   | 4.25                    | 23.2            | 8.31            | $4.39 \times 10^{36}$ | Unknown                     |
| 153                 | 01:33:39.71 30:32:29.2 | 7.12                   | 3.14                    | 61.7            | 159.            | $2.14 \times 10^{38}$ | Cluster                     |
| 172                 | 01:33:43.85 30:32:10.4 | 8.06                   | 4.31                    | 42.0            | 200.            | $2.82 \times 10^{38}$ | Cluster                     |
| 176                 | 01:33:44.51 30:37:52.7 | 8.26                   | 4.45                    | 34.1            | 65.5            | $8.54 \times 10^{37}$ | Unknown                     |
| 181                 | 01:33:45.80 30:27:17.3 | 7.18                   | 3.20                    | 14.9            | 11.6            | $1.21 \times 10^{37}$ | Cluster                     |
| 194                 | 01:33:50.70 30:58:50.3 | 7.28                   | 3.67                    | 7.28            | 2.79            | $1.66 \times 10^{36}$ | Cluster                     |
| 195                 | 01:33:50.73 30:44:56.2 | 7.81                   | 3.59                    | 20.0            | 28.8            | $3.58 \times 10^{37}$ | Cluster                     |
| 197                 | 01:33:50.85 30:38:34.5 | 7.22                   | 4.24                    | 29.3            | 34.0            | $4.03 \times 10^{37}$ | Cluster                     |
| 198                 | 01:33:50.90 30:38:55.5 | 6.86                   | 3.68                    | 110.            | 66.4            | $6.08 \times 10^{37}$ | Cluster                     |
| 201                 | 01:33:51.24 30:34:13.2 | 6.96                   | 3.00                    | 14.8            | 45.7            | $6.25 \times 10^{37}$ | Cluster                     |
| 214                 | 01:33:53.69 30:48:21.5 | 7.72                   | 4.11                    | 15.4            | 8.9             | $7.99 \times 10^{36}$ | Cluster                     |
| 215                 | 01:33:54.10 30:33:09.7 | 7.32                   | 3.87                    | 49.4            | 621.            | $9.03 \times 10^{38}$ | Cluster                     |
| 217                 | 01:33:54.63 30:34:48.3 | 6.94                   | 2.84                    | 47.9            | 104.            | $1.38 \times 10^{38}$ | Cluster                     |
| 219                 | 01:33:54.75 30:45:28.4 | 6.62                   | 2.98                    | 2.92            | 85.6            | $1.26 \times 10^{38}$ | Cluster                     |
| 222                 | 01:33:55.18 30:47:58.0 | 7.70                   | 4.42                    | 28.1            | 47.9            | $6.12 \times 10^{37}$ | Cluster                     |
| 228                 | 01:33:56.18 30:38:39.8 | 6.94                   | 3.24                    | 44.3            | 39.2            | $4.30 \times 10^{37}$ | Cluster                     |
| 229                 | 01:33:56.21 30:45:51.8 | 8.01                   | 3.83                    | 18.0            | 45.3            | $6.09 \times 10^{37}$ | Cluster                     |
| 243                 | 01:33:57.87 30:33:25.7 | 7.18                   | 3.90                    | 68.3            | 62.5            | $6.92 \times 10^{37}$ | Cluster                     |
| 246                 | 01:33:58.03 30:39:26.2 | 7.24                   | 3.68                    | 43.9            | 90.9            | $1.20 \times 10^{38}$ | Cluster                     |
| 250                 | 01:33:58.86 30:34:43.2 | 8.01                   | 3.70                    | 43.3            | 131.            | $1.79 \times 10^{38}$ | Cluster                     |

Table 1 continued on next page

Table 1 (continued)

| Region <sup>a</sup> | RA, DEC <sup>a</sup>   | Log (Age) <sup>a</sup> | Log (Mass) <sup>a</sup> | $f_{3.6}^b$ | $f_{8.0}^b$ | $L_{8.0}^c$           | Classification <sup>a</sup> |
|---------------------|------------------------|------------------------|-------------------------|-------------|-------------|-----------------------|-----------------------------|
|                     | (J2000)                | (yrs)                  | ( $M_{\odot}$ )         | (MJy/sr)    | (MJy/sr)    | ergs/s                |                             |
| (1)                 | (2)                    | (3)                    | (4)                     | (5)         | (6)         | (7)                   | (8)                         |
| 255                 | 01:33:59.52 30:45:49.9 | 6.88                   | 3.72                    | 38.8        | 69.6        | $8.98 \times 10^{37}$ | Cluster                     |
| 257                 | 01:33:59.74 30:41:24.4 | 6.68                   | 3.17                    | 3.83        | 206.        | $3.04 \times 10^{38}$ | Cluster                     |
| 260                 | 01:34:00.01 30:33:54.3 | 6.98                   | 3.99                    | 146.        | 55.6        | $3.26 \times 10^{37}$ | Cluster                     |
| 269                 | 01:34:01.60 30:42:31.1 | 6.62                   | 3.00                    | 12.7        | 4.98        | $3.05 \times 10^{36}$ | Unknown                     |
| 271                 | 01:34:01.75 30:32:25.7 | 8.51                   | 4.16                    | 22.7        | 25.5        | $3.00 \times 10^{37}$ | Cluster                     |
| 272                 | 01:34:01.99 30:38:10.9 | 6.62                   | 2.96                    | 12.5        | 4.93        | $3.03 \times 10^{35}$ | Cluster                     |
| 276                 | 01:34:02.48 30:38:41.1 | 7.18                   | 3.83                    | 90.2        | 1427.       | $2.08 \times 10^{39}$ | Unknown                     |
| 280                 | 01:34:02.79 30:46:36.8 | 7.00                   | 3.28                    | 35.7        | 201         | $2.85 \times 10^{38}$ | Unknown                     |
| 288                 | 01:34:03.83 30:29:33.5 | 8.51                   | 4.18                    | 23.4        | 7.68        | $3.40 \times 10^{36}$ | Unknown                     |
| 310                 | 01:34:07.28 30:38:29.5 | 8.01                   | 3.79                    | 13.0        | 6.44        | $5.12 \times 10^{36}$ | Cluster                     |
| 320                 | 01:34:08.53 30:39:02.4 | 6.66                   | 3.91                    | 45.3        | 164.        | $2.27 \times 10^{38}$ | Cluster                     |
| 325                 | 01:34:08.96 30:36:33.8 | 6.88                   | 3.12                    | 66.4        | 40.1        | $3.67 \times 10^{37}$ | Unknown                     |
| 329                 | 01:34:10.09 30:45:29.4 | 6.96                   | 3.33                    | 38.1        | 25.8        | $2.52 \times 10^{37}$ | Cluster                     |
| 335                 | 01:34:11.35 30:41:27.9 | 8.56                   | 4.35                    | 10.1        | 23.3        | $3.11 \times 10^{37}$ | Cluster                     |
| 336                 | 01:34:11.36 30:41:27.9 | 8.56                   | 4.35                    | 9.63        | 22.1        | $2.94 \times 10^{37}$ | Unknown                     |
| 347                 | 01:34:14.02 30:39:29.5 | 8.01                   | 3.93                    | 14.8        | 15.2        | $1.74 \times 10^{37}$ | Cluster                     |
| 351                 | 01:34:14.65 30:32:35.0 | 8.56                   | 4.35                    | 11.6        | 4.2         | $2.18 \times 10^{36}$ | Cluster                     |
| 355                 | 01:34:15.51 30:42:11.5 | 8.51                   | 4.58                    | 44.5        | 22.2        | $1.77 \times 10^{37}$ | Cluster                     |
| 361                 | 01:34:17.54 30:42:36.7 | 7.48                   | 3.00                    | 7.51        | 21.6        | $2.95 \times 10^{37}$ | Cluster                     |
| 370                 | 01:34:19.44 30:46:21.2 | 8.06                   | 4.57                    | 29.2        | 8.33        | $2.39 \times 10^{36}$ | Unknown                     |
| 372                 | 01:34:20.17 30:39:33.3 | 6.96                   | 3.00                    | 9.29        | 20.6        | $2.73 \times 10^{37}$ | Cluster                     |
| 410                 | 01:34:33.09 30:37:36.3 | 6.80                   | 2.97                    | 9.13        | 16.0        | $2.05 \times 10^{37}$ | Cluster                     |
| 420                 | 01:34:40.41 30:46:01.3 | 6.94                   | 3.99                    | 220.        | 190.        | $2.07 \times 10^{38}$ | Cluster                     |
| 422                 | 01:34:40.72 30:53:02.0 | 6.94                   | 2.63                    | 31.3        | 21.9        | $2.18 \times 10^{37}$ | Cluster                     |
| 439                 | 01:34:50.10 30:47:04.1 | 8.06                   | 4.67                    | 29.9        | 7.68        | $1.18 \times 10^{36}$ | Cluster                     |

NOTE—<sup>a</sup> IDs, coordinates, ages, masses and classifications from Sarajedini & Mancone (2007). Masses are rescaled to our adopted distance of 850 kpc for M33, which is slightly smaller than the one used by Sarajedini & Mancone (2007).

NOTE—<sup>b</sup> Flux density measured in the  $5''$  radius photometric aperture, uncorrected for any aperture effect.

NOTE—<sup>c</sup> Calculated for the adopted distance of 850 kpc for M33. The values listed include all corrections described in Sec 3.

## REFERENCES

- Adamo, A., & Bastian, N. 2018, The Lifecycle of Clusters in Galaxies, ed. S. Stahler, Vol. 424, 91
- Adamo, A., Ryon, J. E., Messa, M., et al. 2017, ApJ, 841, 131
- Aniano, G., Draine, B. T., Hunt, L. K., et al. 2020, ApJ, 889, 150
- Asplund, M., Grevesse, N., Sauval, A. J., & Scott, P. 2009, ARA&A, 47, 481
- Bastian, N., & Lardo, C. 2018, ARA&A, 56, 83
- Bendo, G. J., Draine, B. T., Engelbracht, C. W., et al. 2008, MNRAS, 389, 629
- Binder, B. A., & Povich, M. S. 2018, ApJ, 864, 136
- Boselli, A., Lequeux, J., & Gavazzi, G. 2004, A&A, 428, 409

- Bresolin, F. 2011, *ApJ*, 730, 129
- Brown, G., & Gnedin, O. Y. 2021, *MNRAS*, 508, 5935
- Calapa, M. D., Calzetti, D., Draine, B. T., et al. 2014, *ApJ*, 784, 130
- Calzetti, D., Kennicutt, R. C., Engelbracht, C. W., et al. 2007, *ApJ*, 666, 870
- Calzetti, D., Lee, J. C., Sabbi, E., et al. 2015, *AJ*, 149, 51
- Corbelli, E., & Salucci, P. 2000, *MNRAS*, 311, 441
- Crocker, A. F., Calzetti, D., Thilker, D. A., et al. 2013, *ApJ*, 762, 79
- Dale, D. A., Cohen, S. A., Johnson, L. C., et al. 2009, *ApJ*, 703, 517
- Draine, B. T., & Li, A. 2007, *ApJ*, 657, 810
- Draine, B. T., Li, A., Hensley, B. S., et al. 2020, arXiv e-prints, arXiv:2011.07046
- Elbaz, D., Dickinson, M., Hwang, H. S., et al. 2011, *A&A*, 533, A119
- Engelbracht, C. W., Rieke, G. H., Gordon, K. D., et al. 2008, *ApJ*, 678, 804
- Fazio, G. G., Hora, J. L., Allen, L. E., et al. 2004, *ApJS*, 154, 10
- Ferrarese, L., Mould, J. R., Kennicutt, Robert C., J., et al. 2000, *ApJ*, 529, 745
- Gordon, K. D., Engelbracht, C. W., Rieke, G. H., et al. 2008, *ApJ*, 682, 336
- Helou, G., Roussel, H., Appleton, P., et al. 2004, *ApJS*, 154, 253
- Kennicutt, Robert C., J., Hao, C.-N., Calzetti, D., et al. 2009, *ApJ*, 703, 1672
- Kennicutt, R. C., & Evans, N. J. 2012, *ARAA*, 50, 531
- Lawton, B., Gordon, K. D., Babler, B., et al. 2010, *ApJ*, 716, 453
- Lebouteiller, V., Bernard-Salas, J., Whelan, D. G., et al. 2011, *ApJ*, 728, 45
- Leger, A., & Puget, J. L. 1984, *A&A*, 500, 279
- Leitherer, C., Schaerer, D., Goldader, J. D., et al. 1999, *ApJS*, 123, 3
- Lin, Z., Hu, N., Kong, X., et al. 2017, *ApJ*, 842, 97
- Lin, Z., Calzetti, D., Kong, X., et al. 2020, *ApJ*, 896, 16
- Lu, N., Bendo, G. J., Boselli, A., et al. 2014, *ApJ*, 797, 129
- Ma, J., Zhou, X., Kong, X., et al. 2001, *AJ*, 122, 1796
- Madden, S. C., Galliano, F., Jones, A. P., & Sauvage, M. 2006, *A&A*, 446, 877
- McQuinn, K. B. W., Woodward, C. E., Willner, S. P., et al. 2007, *ApJ*, 664, 850
- Moeller, C., & Calzetti, D. 2022, *AJ*, 163, 16
- Povich, M. S., Stone, J. M., Churchwell, E., et al. 2007, *ApJ*, 660, 346
- Querejeta, M., Meidt, S. E., Schinnerer, E., et al. 2015, *ApJS*, 219, 5
- Reddy, N. A., Erb, D. K., Pettini, M., Steidel, C. C., & Shapley, A. E. 2010, *ApJ*, 712, 1070
- Reddy, N. A., Steidel, C. C., Fadda, D., et al. 2006, *ApJ*, 644, 792
- Relaño, M., & Kennicutt, Robert C., J. 2009, *ApJ*, 699, 1125
- Ryon, J. E., Gallagher, J. S., Smith, L. J., et al. 2017, *ApJ*, 841, 92
- Sandstrom, K. M., Bolatto, A. D., Bot, C., et al. 2012, *ApJ*, 744, 20
- Sarajedini, A., & Mancone, C. L. 2007, *AJ*, 134, 447
- Shiple, H. V., Papovich, C., Rieke, G. H., Brown, M. J. I., & Moustakas, J. 2016, *ApJ*, 818, 60
- Shivaei, I., Reddy, N. A., Steidel, C. C., & Shapley, A. E. 2015, *Apj*, 804, 149
- Shivaei, I., Reddy, N. A., Shapley, A. E., et al. 2017, *ApJ*, 837, 157
- Smith, J. D. T., Draine, B. T., Dale, D. A., et al. 2007, *ApJ*, 656, 770
- Tielens, A. G. G. M. 2008, *ARA&A*, 46, 289
- . 2013, *Reviews of Modern Physics*, 85, 1021
- Toribio San Cipriano, L., García-Rojas, J., Esteban, C., Bresolin, F., & Peimbert, M. 2016, *MNRAS*, 458, 1866
- U, V., Urbaneja, M. A., Kudritzki, R.-P., et al. 2009, *ApJ*, 704, 1120
- Vázquez, G. A., & Leitherer, C. 2005, *ApJ*, 621, 695
- Verley, S., Corbelli, E., Giovanardi, C., & Hunt, L. K. 2009, *A&A*, 493, 453
- Weisz, D. R., Johnson, B. D., Johnson, L. C., et al. 2012, *ApJ*, 744, 44
- Werner, M. W., Roellig, T. L., Low, F. J., et al. 2004, *ApJS*, 154, 1
- Whitmore, B. C., Chandar, R., Kim, H., et al. 2011, *ApJ*, 729, 78
- Whitmore, B. C., Chandar, R., Lee, J., et al. 2020, *ApJ*, 889, 154
- Wofford, A., Charlot, S., Bruzual, G., et al. 2016, *MNRAS*, 457, 4296
- Wu, H., Cao, C., Hao, C.-N., et al. 2005, *ApJL*, 632, L79